PCCP

PAPER

View Article Online
View Journal | View Issue



Cite this: *Phys. Chem. Chem. Phys.*, 2024, **26**, 5669

# AsymPol-TEKs as efficient polarizing agents for MAS-DNP in glass matrices of non-aqueous solvents†

Rania Harrabi,[a] Thomas Halbritter,[b] Shadi Alarab,[a] Satyaki Chatterjee,[b] Malgorzata Wolska-Pietkiewicz,[c] Krishna K. Damodaran,[b] Johan van Tol,[d] Daniel Lee,‡[a] Subhradip Paul,[a] Sabine Hediger,[a] Snorri Th. Sigurdsson,*[b] Frederic Mentink-Vigier*[d] and Gaël De Paëpe*[a]

Two polarizing agents from the AsymPol family, **AsymPol-TEK** and **cAsymPol-TEK** (methyl-free version) are introduced for MAS-DNP applications in non-aqueous solvents. The performance of these new biradicals is rationalized in detail using a combination of electron paramagnetic resonance spectroscopy, density functional theory, molecular dynamics and quantitative MAS-DNP spin dynamics simulations. By slightly modifying the experimental protocol to keep the sample temperature low at insertion, we are able to obtain reproducable DNP-NMR data with 1,1,2,2-tetrachloroethane (TCE) at 100 K, which facilitates optimization and comparison of different polarizing agents. At intermediate magnetic fields, **AsymPol-TEK** and **cAsymPol-TEK** provide 1.5 to 3-fold improvement in sensitivity compared to **TEKPol**, one of the most widely used polarizing agents for organic solvents, with significantly shorter DNP build-up times of ~1 s and ~2 s at 9.4 and 14.1 T respectively. In the course of the work, we also isolated and characterized two diastereoisomers that can form during the synthesis of **AsymPol-TEK**; their difference in performance is described and discussed. Finally, the advantages of the **AsymPol-TEKs** are demonstrated by recording 2D $^{13}C$–$^{13}C$ correlation experiments at natural $^{13}C$-abundance of proton-dense microcrystals and by polarizing the surface of ZnO nanocrystals (NCs) coated with diphenyl phosphate ligands. For those experiments, **cAsymPol-TEK** yielded a three-fold increase in sensitivity compared to **TEKPol**, corresponding to a nine-fold time saving.

Received 4th September 2023,
Accepted 22nd January 2024

DOI: 10.1039/d3cp04271e

rsc.li/pccp



## Introduction

Magic angle spinning dynamic nuclear polarization (MAS-DNP) has expanded the scope of solid-state Nuclear Magnetic Resonance (ssNMR) spectroscopy.[1–6] MAS-DNP boosts $^{1}H$ spin polarization by taking advantage of the higher polarization of unpaired electrons spins that are present in so-called Polarizing Agents (PAs).[7,8] This results in an improved sensitivity that enables applications to challenging materials and the study of complex biomolecular systems.[9–20]

Several DNP mechanisms have been reported at high magnetic fields, including the solid effect, the Overhauser effect, and the cross effect.[2] The cross-effect (CE) is currently the most efficient in terms of sensitivity[3,21–24] and necessitates the use of PAs containing two coupled electron spins.[7] The electron spin polarization difference is transferred to the isotope of interest *via* a complex mechanism driven by the sample spinning and microwave (μw) irradiation[3,5,25–34] at cryogenic temperature (typically ~100 K[35,36] or lower[4,37–44]). However, further improvements remain mandatory to fully unlock the potential of MAS-DNP especially for challenging samples, and at high magnetic fields and fast MAS frequencies. This has triggered the continuous development of PAs for MAS-DNP, from the introduction of improved bis-nitroxides[45–49] to hetero-biradicals such as trityl-nitroxides[50–55] and BDPA-nitroxides.[56,57]

PAs are designed for use in either aqueous matrices or in organic solvents, depending on the systems studied. The use in organic solvents is critical for systems that are incompatible

[a] *Univ. Grenoble Alpes, CEA, CNRS, IRIG, MEM, 38000 Grenoble, France. E-mail: gael.depaepe@cea.fr*
[b] *University of Iceland, Department of Chemistry, Science Institute, Dunhaga 3, 107 Reykjavik, Iceland. E-mail: snorrisi@hi.is*
[c] *Faculty of Chemistry, Warsaw University of Technology, Noakowskiego 3, 00-664 Warsaw, Poland*
[d] *National High Magnetic Field Laboratory, Florida State University, Tallahassee, FL 32301, USA. E-mail: fmentink@magnet.fsu.edu*

† Electronic supplementary information (ESI) available. See DOI: https://doi.org/10.1039/d3cp04271e

‡ Current address: Department of Chemical Engineering, University of Manchester, Manchester, M13 9PL, UK.

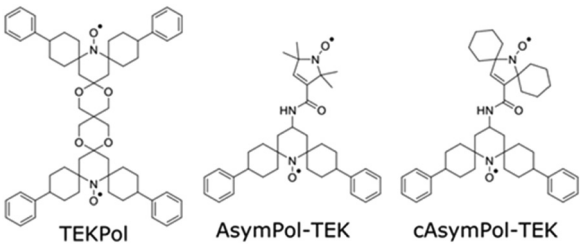


Fig. 1 Structures of **TEKPol**, **AsymPol-TEK**, and **cAsymPol-TEK**.

with water.[16,19,58] The development of PAs for organic solvents is thus vital for many applications, and the specific challenges associated with the use of these solvents must be overcome. A few PAs have been described for MAS-DNP applications in organic solvents. The bTbK family,[48,59–61] which includes **TEKPol**[48] (Fig. 1) and NaphPol,[61] along with the heterobiradicals HyTEK-2[57] and PyrroTriPol-OMe[54] are so far the best PAs for MAS-DNP experiments in non-aqueous solvents. At intermediate fields (9.4 and 14.1 T), PAs based on bis-nitroxides are still a good option, owing to their relative hyperpolarization efficiency, more facile synthesis, and ease of tuning the performance by chemically-controlling the e–e couplings and the *g*-tensor relative orientation.[45,46,49] However, the bTbK family is less efficient at high magnetic field and fast MAS frequencies,[56] in part due to their relatively weak electron–electron (e–e) coupling.[27,28,34,48,62] The weak coupling is also responsible for a large depolarization effect[28,31,34] and a longer hyperpolarization build-up time.[28,34] To go beyond the performance of the bTbK family, it is necessary to make new biradicals with stronger e–e couplings that can quickly generate large nuclear hyperpolarization, even for samples with large proton concentration,[49] and/or under high spinning frequencies.[27,45,51] This strategy has previously been applied to the AsymPol radical family, which was shown to provide excellent DNP performance in aqueous solutions (AsymPol-POK and cAsymPol-POK)[45,49] due to a sizable e–e coupling and a near orthogonal relative orientation of the two nitroxides.[28,29]

Here we describe the synthesis and characterization of two new members of the AsymPol family, **AsymPol-TEK** and **cAsymPol-TEK** (Fig. 1). for use in organic solvents. Interestingly, the synthesis yields two stereoisomers that do not provide the same DNP efficiency. Focusing on the better performing isomer, we show that **AsymPol-TEK** and **cAsymPol-TEK** have a higher DNP efficiency than **TEKPol**, thanks to their very fast build-up at both 9.4 and 14.1 T. Their performance is rationalized by a combination of DFT computations, electron paramagnetic resonance (EPR) experiments, molecular dynamics simulations (MD) and a predictive numerical model.[30,33,49] In particular, DFT and multi-frequency EPR simulations enable estimating the electron dipolar coupling, the exchange interactions ($J$), the relative orientation of the *g*-tensors, and the ratio of the two main conformers.

For MAS-DNP applications, the solvent matrix must form a glass at cryogenic temperature to provide adequate spin relaxation properties and ensure a uniform distribution of the PAs.[4,63] In addition, the $^1$H nuclei of the solvent must relax slowly. Only a handful of organic solvents have proven suitable for MAS-DNP experiments[58] and 1,1,2,2-tetrachloroethane (TCE), is currently one of the most used.[16,18,58,64–67] Nevertheless TCE remains challenging to use and several factors affect the DNP efficiency when using it.[58,68,69] It can form a glass phase at 100 K with rapid cooling of the sample, but crystalline phases can also be generated between 100 K and 200 K. Chlorinated solvent can dissolve a large amount of $O_2$ at room temperature (tens of mM)[70,71] which enhances the $^1$H relaxation rate and lowers the DNP efficiency. Degassing or packing of the sample under inert atmosphere is often used to overcome this problem.[66,68,72]

We thus addressed sample preparation, which is important for optimal DNP results. We confirmed that minimizing the oxygen content of the sample is important for **TEKPol** but less for the **AsymPol-TEKs** and demonstrate the critical importance to insert the sample into a probe sufficiently cold ($\sim$100 K or lower). The commonly used freeze–thaw cycle procedure[68] was modified to introduce the sample in absence of μw irradiation. Slightly higher probe temperatures, *e.g.* $>$ 110 K, have a direct impact on the glass quality and DNP efficiency. This approach drastically improves the reproducibility of the DNP-NMR data and solves one of the problems associated with the use of TCE thus far. Finally, we illustrate the performance of the **AsymPol-TEKs** by reporting 2D $^{13}$C–$^{13}$C correlation experiments at natural $^{13}$C-abundance of proton-dense microcrystals and to hyperpolarize the surface of ZnO nanocrystals (NCs). For those experiments, **cAsymPol-TEK** yielded a three-fold increase in sensitivity compared to **TEKPol**, corresponding to a nine-fold time saving.

## Material and methods

### Sample preparation for MAS-DNP experiments

**TEKPol** was purchased from Cortecnet; **AsymPol-TEK** and **cAsymPol-TEK** (Fig. 1) were synthesized as described below. 10 $\pm$ 0.5 and 16 $\pm$ 0.5 mM solutions of **TEKPol**, **AsymPol-TEK** and **cAsymPol-TEK** were prepared in non-deuterated 1,1,2,2-tetrachloroethane (TCE). Hexagonal boron nitride (h-BN), adenosine and caffeine powders were purchased from Sigma-Aldrich and used as received without further purification. For the tests on the TCE solvent itself, 30 mg of h-BN was mixed with 30 μL of 10 or 16 mM **TEKPol**, **AsymPol-TEK**, **cAsymPol-TEK** in TCE. For the experiments on organic microcrystals, 30 mg of caffeine or adenosine powder were impregnated with 25 μL of 10 mM radical solution in TCE. The total weight of sample inside the rotor was estimated to be $\sim$25 mg, by weighing the rotor before and after the sample was packed. For the DNP experiments on the ZnO nanocrystals coated with monoanionic diphenyl phosphate (DPP) ligands, the ZnO NC powder was heated at a temperature of 90 °C for 14 h, and then subsequently impregnated with 10 mM **cAsymPol-TEK** in TCE, before being packed into a 3.2 mm sapphire rotor.

### MAS-DNP experiments

Experiments were carried out at CEA-Grenoble (Grenoble, France) on a Bruker 9.4 T/400 MHz ($^1$H frequency)/263 GHz

 

(electron frequency)[35] and at the National MagLab (Tallahassee, USA) on the 14.1 T/600 MHz/395 GHz MAS-DNP setup.[73] Both instruments are equipped with a Bruker Avance III console and a 3.2 mm wide-bore MAS-DNP probe capable of doing MAS NMR at 100 K. All samples were packed into 3.2 mm sapphire rotors and closed with Vespel caps. On the 600 MHz DNP setup, the μw power and the Martin-Puplett interferometer position were adapted to maximize the DNP effect.[41,73] To characterize the MAS-DNP performance, the $^{13}$C signal intensity of either the solvent TCE or the impregnated powders was measured through a $^{1}$H–$^{13}$C CP experiment. Except if specified otherwise, a 100 kHz RF field was used for $^{1}$H decoupling. A 1 to 2 ms ramped (80 to 100%) CP was used on the $^{1}$H channel to match a Hartman-Hahn CP condition, with the $^{13}$C RF field strength set to 50 kHz. The polarization build-up time $T_B$ was obtained from proton saturation-recovery experiments under μw irradiation. The DNP enhancement factor $\varepsilon_{on/off}$, the depolarization factor $\varepsilon_{depo}$ and the sensitivity were measured according to previous protocols.[49] Additional details can be found in the ESI.†

### Modified freeze–thaw cycle procedure with TCE

To test the repeatability of the measurements on samples containing TCE, a freeze–thaw cycle was performed between each repeated experiment, using the following procedure. The rotor was ejected and kept either in the rotor catcher inside the probe base or on the bench. The μw irradiation was then turned off, while the bearing and drive pressures were raised to 800 mbar and the VT maintained to the same level as for the experiments. After 5 minutes, the rotor was inserted again in the cold probe head. We observed that keeping the μw off while inserting and spinning up the sample is critical to optimize the glass formation as it avoids heating the sample and generating crystalline phases.

### Electron paramagnetic resonance (EPR) experiments

Continuous wave (CW) EPR measurements were carried out at 9.6 and 240 GHz electron resonance, both at a temperature of 100 K. At 9.6 GHz, samples were measured inside the sapphire rotor on an EMX-Nano using a $N_2$ cooled Dewar. The field modulation was set to 0.1 mT and the μw power to 1 μW to avoid signal saturation. The 240 GHz spectrum were measured under the same conditions as previously described.[33,49,54,74] The field modulation was set to 0.3 mT and the μw power was reduced in order to avoid signal saturation. The calibration of the magnetic field allows the determination of the *g*-values with a global uncertainty of $2 \times 10^{-4}$.[30,33,49]

### MAS-DNP simulations

Simulations were performed with the latest implementation of a previously published method that uses a combination of Bloch and Landau–Zener evolution operators in Liouville space.[28,30,33,49] With this model, the computational time scales linearly with the number of spins. It has been improved to take into account large dipolar and exchange interactions[49] but also accurately describe the spin diffusion around the biradicals.[33]

The ''multi-nuclei'' model simulates an isolated biradical in interaction with many protons (from the radical and the solvent). This model uses as input MD simulations carried out in explicit TCE. It accounts for the presence of solvent protons but also biradical protons and their isotropic and anisotropic hyperfine couplings obtained by DFT. The simulations were carried out for both conformers and the polarization build-ups were weighted-averaged to mimic experimental results.

Nevertheless, it is important to note that the results obtained with the multi-nuclei model (build-up times and final polarization) do not consider the presence of intermolecular electron–electron couplings. Following our previous work,[30,33,49] we can use a second model, called the ''box model'' to correct the results obtained with the multi nuclei model. The ''box'' model uses *N* copies of a three-spin system (2 electrons, 1 proton) randomly distributed in a box to match a given biradical concentration. Assuming that ''intermolecular'' cross-effect is negligible, the effect of biradical concentration can be calculated by comparing the results of the box model with and without intermolecular electron–electron couplings. The simulated $\varepsilon_{on/off}$, $\varepsilon_B$ and $\varepsilon_{depo}$ can be written as follows:

$$\varepsilon_X^{sim} = \varepsilon_X^{multi\text{-}nuclei} \times \frac{\varepsilon_X^{Box/Interacting}}{\varepsilon_X^{Box/Isolated}} = \varepsilon_X^{multi\text{-}nuclei} \times R_X^{Box}$$

where $R_X^{Box}$ corresponds to a correction factor accounting for the biradical concentration. This is justified for homogenously distributed biradicals in the tens of millimolar range as intermolecular cross-effect rotor events are then particularly weak.[27,28,31] This approach has been shown to provide $\varepsilon_{on/off}$, $\varepsilon_B$ and $\varepsilon_{depo}$ values that are relatively close to experimental ones for **TEKPol**, AMUPol and AsymPol-POK.[30,33] More details about the parameters used in the simulations can be found in the ESI.†

### DFT simulations

Except otherwise specified, the DFT computations were carried out *via* Orca 5.0.[75] The preliminary structures were generated and optimized using Avogadro v1.2.[76] The structures were optimized using r2SCAN-3c.[77] A Polarizable Continuum Model Chloroform (PCM (Chloroform))[78] was used to mimic the dielectric properties of TCE. The *g*-tensors, dipolar interaction and hyperfine couplings were computed using PBE0,[79] def2-TZVP.[80] The hyperfine coupling to either electron *a* or *b* were computed, bearing in mind that accurate determination is beyond the scope of this article.[81] The Gauge origin problem was sorted out using the origin as the spin density. The exchange interaction was computed using the range-separated functional ωB97M-D4,[82,83] the def2-SVP basis, and a very tight and slow convergence ($10^{-10}$ Hartree).[84]

### EPR simulations

The EPR spectra were computed using Easyspin 5.2.20[85] *via* the Hamiltonian diagonalization method (''matrix''). The line broadening used, corresponding to a *g*-strain proportional to $[2(g_{xx} - 2), g_{yy} - 2, g_{zz} - 2] \times 7\%$, and a mixture of Gaussian and Lorentzian lineshapes with linewidth of 0.4 and 0.4 mT respectively. The EPR spectra were fitted using the DFT-predicted parameters as starting points. The *g*-values were first adjusted,

and then the conformer ratio. Finally, *g*-tensors' Euler angles and the magnitude of the *J*-exchange interaction were refined together. The Euler angles of the dipolar interaction were fixed as they had very little impact on the fits. For the fitting procedure, a weighting factor of 1 for the 9.6 GHz (X-band) spectrum and of 2 for the 240 GHz spectrum was applied, giving thus a higher contribution of the high field EPR spectrum fit to the least-square sum and therefore forcing a better agreement with the high field spectrum with respect to the low field one for the extraction of the *g*-tensor relative orientation. Indeed, the low field EPR spectrum is dominated by the dipolar/exchange interaction and the $^{14}$N hyperfine coupling while the high field spectrum is sensitive to the biradical geometry and *g*-tensor relative orientation. When multiple reasonable fits were obtained, the best one was chosen based on its match with the low field spectral features (resonant positions and relative intensities).

### Molecular dynamics (MD) simulations

MD simulations were carried out using OpenMM[86] and the AMBER[87] (GAFF2) force field. For the nitroxide, the force field derived by Barone's group[88] was adapted to match the GAFF2 atom type.[89] Lone pairs were added to NO in order to faithfully represent hydrogen bonding occurring in the solvent[88] and an additional dihedral angle was included in the force field as previously described.[90] The charges were obtained from the DFT structures, using the two-steps RESP fitting procedure with Multiwfn[91] to provide reliable MD structures. The MD simulations were carried out in explicit TCE (including bond rotation), whose charges were obtained on the same way. The MD simulations used as input for MAS-DNP simulations, consisted in first minimizing the energy of the molecular system, then equilibrating it for 20 ps, and finally propagating it for 100 ns in steps of 1 fs under an assumed pressure of 1 bar and a temperature of 298 K. The set temperature was then quickly decreased to 100 K over 400 ps to simulate freezing and glass formation.

## Results and discussion

The AsymPols are bisnitroxides made of a piperidine-based radical linked to a pyrrolinoxyl radical *via* an amide bridge.[45,49] **AsymPol-TEK** and **cAsymPol-TEK** (Fig. 1) contain features that were previously introduced with bcTbK and **TEKPol**.[48] Specifically, spirocyclohexyl groups flank the nitroxide of the piperidine ring to slow the electron relaxation times, and phenyl groups contribute to higher solubility in organic solvents. The electron relaxation times of **cAsymPol-TEK** were further slowed down by introduction of spirocyclohexyl groups on the five-membered pyrroline ring, which also increase the molecular weight.[47,48,92,93]

### Synthesis of AsymPol-TEK and cAsymPol-TEK

The synthesis of **AsymPol-TEK** and **cAsymPol-TEK** (Scheme 1) followed closely that of AsymPol.[45] Conjugation of nitroxide **1**[94] to 3-carboxy-pyrrolinoxyl **2**[95] provided **AsymPol-TEK** in good yields. HPLC analysis revealed the presence of two diastereomers. The origin of the stereoisomerism is the configuration of the two cyclohexane carbon atoms bearing the phenyl substituents. Relative to the cyclohexane rings, a phenyl group has either a *cis*- or *trans*-relationship to the nitrogen at the spirocycle junction. This can result in three diastereomers, namely the *cis–cis*, *cis–trans* and *trans–trans*. Only two diastereomers, named isomer A and isomer B, were observed and isolated by chromatography (ESI†). Isomer A (*cis–cis*) crystallized readily and the crystal structure showed that the two benzene rings were in equatorial position with respect to the cyclohexyl rings, with an ''open–open'' conformation relative to the N–O group (see ESI†).[96] In spite of several attempts, we were not able to crystallize isomer B. For **AsymPol-TEK**, except specified otherwise, all DNP experiments were conducted on isomer A. **cAsymPol-TEK** was synthesized in an analogous manner to **AsymPol-TEK** by condensation of **1** with spirocyclohexyl-3-carboxypyrrolinoxyl **3**.[95] In this case, only one peak was observed by HPLC analysis, indicating a single isomer. The crystal structure of **cAsymPol-TEK** revealed a *cis–cis* isomer in which the two benzene rings in are in equatorial positions with an ''open–open'' conformation relative to the N–O group (see ESI†).

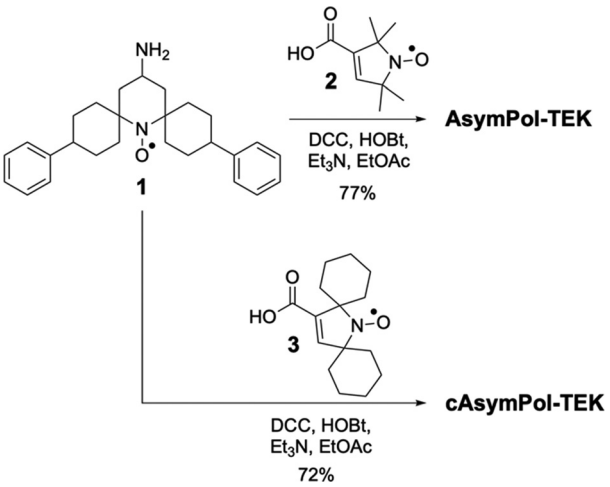


Scheme 1 Synthesis of **AsymPol-TEK** and **cAsymPol-TEK**.

### Geometry of AsymPol-TEK and cAsymPol-TEK

The structures of the biradicals **AsymPol-TEK** and **cAsymPol-TEK** in frozen solution were determined using DFT calculations. After obtaining the idealized geometry of each biradical and the corresponding magnetic properties (*g*-tensors, exchange interaction and dipolar couplings), the latter were used as initial parameters to fit the EPR spectra.[30,33,49] While the planarity of the peptide bond (*i.e.* H–N–C═O) is maintained, the steric hindrance between the N–H proton and the C═C–H proton of the five-membered ring prevents the carbonyl bond and the double bond (*i.e.* O═C–C═C) from being in the same plane. As a result, **AsymPol-TEK** and **cAsymPol-TEK** each contain two major conformers, dubbed **#1** and **#2**, that have a different

 

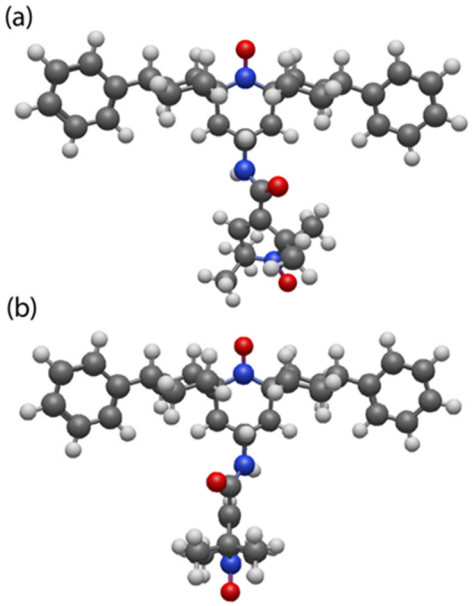


Fig. 2 3D representation of the two open–open conformers of **AsymPol-TEK** (a) conformer **#1**, (b) conformer **#2**.

relative orientation between the five and six membered rings, shown in Fig. 2 for **AsymPol-TEK**.

The DFT simulations predict that conformer **#1** is slightly lower in energy than **#2**. The two conformers possess different magnetic properties: a larger *g*-tensors' distance, $L_{a,b}$, is predicted for **#2** *vs.* **#1**, while the anti-ferromagnetic exchange interaction between the two unpaired electrons, $J_{a,b}$, is about +100 MHz for **#1** and +60 MHz for **#2**. Similar predictions were obtained for **cAsymPol-TEK** (Table 1).

To refine the predictions of the DFT calculations, the experimental EPR spectra, recorded at frequencies of 9.6 and 240 GHz, were fitted (see Fig. 3a). At 9.6 GHz, the EPR spectra of **AsymPol-TEK** and **cAsymPol-TEK** are similar, but some minor differences are observed in the high-frequency EPR spectra. These differences are reproducible, despite variations in the glass quality. We note that the high-field EPR spectra differ significantly from those of the AsymPol-POKs in the $g_{yy}$ region, revealing different properties between the POK and TEK versions.

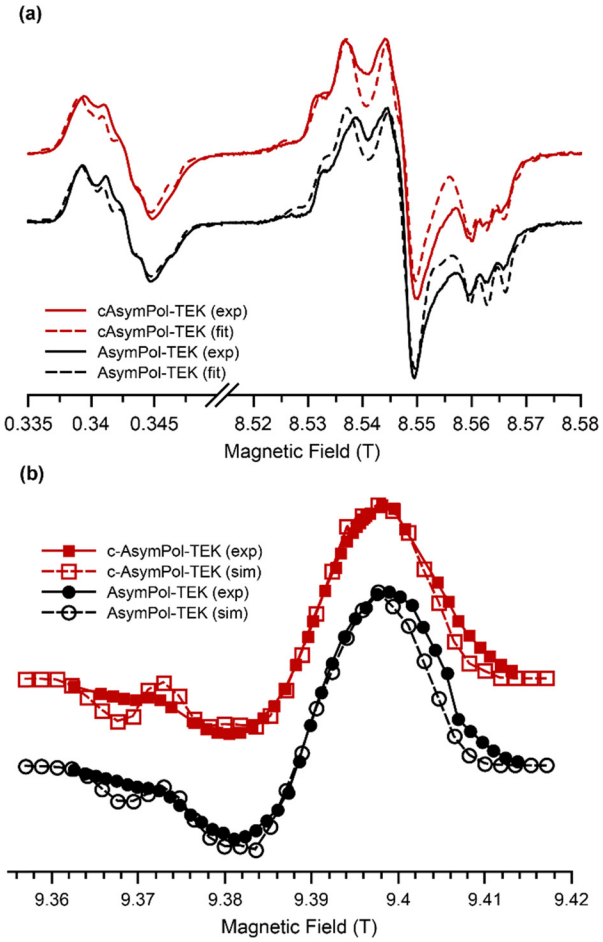


Fig. 3 (a) Experimental (solid lines) and best fit (dashed lines) EPR spectra of **AsymPol-TEK** (black) and **cAsymPol-TEK** (red) in TCE with h-BN, measured at 100 K, 9.6 T and 240 GHz. Note that the experimental spectra are affected by the cooling process. This relates to the difficulty in obtaining a reproducible glassy state with TCE. For the fits, the $^{14}$N hyperfine was set to [15,14,95] MHz for the five- and [18,17,98] MHz for the six-membered ring. (b) Experimental (full symbols) and simulated (open symbols) MAS-DNP field profiles of **AsymPol-TEK** (black circles) and **cAsymPol-TEK** (red squares) measured in TCE with h-BN at 100 K and 263 GHz.

The magnetic/geometric parameters predicted by DFT provided reasonable starting values for the fitting of the EPR

Table 1 List of the calculated (DFT) and fitted magnetic parameters for the **AsymPol-TEK** and **cAsymPol-TEK** biradicals

| Biradical | g-tensors [$g_{xx}$, $g_{yy}$, $g_{zz}$] | g-tensors relative orientation [α,β,γ] [degrees] | Dipolar coupling, exchange interaction [MHz] | Dipolar orientation [ϕ,θ] [degrees][a] | $L_{a,b}$ ($\times 10^3$) |
|---|---|---|---|---|---|
| **AsymPol-TEK #1** DFT/Fit | [2.0090, 2.0060, 2.0021; 2.0095, | [98,148, 129]/[**115,150, 129**] | [58,96]/[**58,95**] | [−19,104] | 4.2/**3.6** |
| **AsymPol-TEK #2** DFT/Fit | 2.0064, 2.0022]/ | [75,85,89]/[**67,73,85**] | [56,61]/[**56,65**] | [−14, 94] | 6.0/**5.8** |
| | [2.0086, 2.0062, 2.0023; 2.0095, 2.0062, 2.0024][b] | | | | |
| **cAsymPol-TEK #1** DFT/Fit | [**2.0089, 2.0060, 2.0021; 2.0095,** | [116,149,152]/[**121,155, 150**] | [60,137]/[**60,105**] | [−20, 108] | 4.8/**4.1** |
| **cAsymPol-TEK #2** DFT/Fit | **2.0064, 2.0022]/** | [76,86,93]/[**76,84,92**] | [56,67]/[**56,60**] | [−12.5, 96] | 5.9/**5.6** |
| | **[2.0089, 2.0060, 2.0022; 2.0098, 2.0061, 2.0024]**[b] | | | | |

[a] Euler angles are given with respect to the *g*-tensor of the five-membered ring, using Easyspin's v5 rotation convention (active rotation). [b] We assumed identical *g*-tensors values for both conformers.

spectra that yielded acceptable agreement with the experimental data (Table 1). Both biradicals present at least the two considered conformers (**#1** and **#2**) that have similar dipolar couplings (between 56 and 60 MHz), but different exchange interactions and different relative orientations. Conformers **#1** and **#2**, are present at a ratio of 60 : 40 for **AsymPol-TEK** and 65 : 35 for **cAsymPol-TEK**. For conformers **#1**, the exchange interactions were found to be 95 and 105 MHz for **AsymPol-TEK** and **cAsymPol-TEK**, respectively, and 65 and 60 MHz for conformers **#2** (see Table 1). These exchange couplings are slightly lower for **AsymPol-TEK**/**cAsymPol-TEK** compared to AsymPol-POK/cAsymPol-POK. This could already be inferred from the liquid-state EPR spectra, which presents a weaker exchange interaction of $|J_{a,b}|$ = 55 MHz (*vs.* 78 MHz for AsymPol-POK) as shown in Fig. S1 (ESI†). This is likely related to interaction with the different solvents, which impacts electron delocalization as revealed by the larger $g_{xx}$ value that correlates with a shift of the unpaired spin-density towards the O (see Table 1). In addition, the relative orientation of the NO groups can affect the overlap between the orbitals of the unpaired electrons and thus the exchange interaction.

The agreement between experiment and simulations was improved with the use of significant *g*-strain (larger than in previous studies),[30,33,49,97] but it remains imperfect. This is likely due both to the lack of precise control of the glass formation and to the fact that the **AsymPol-TEK** radicals possess a distribution of conformations, implying a distribution of exchange interactions.[84,98] The validity of the parameters extracted from the fits was confirmed by comparing experimental and simulated MAS-DNP field profiles (DNP enhancement *versus* magnetic field for a fixed μw frequency), which shows very good agreement (Fig. 3b). The relative ratio between the positive and negative maxima of the DNP field profile is well reproduced, as well as the features at 9.37 T. The field-sweep profiles of **AsymPol-TEK** and **cAsymPol-TEK** are very similar to their POK counterparts. However, there are variations in the 9.36–9.39 T regions, confirming that the TEK versions have lower exchange interactions.[45]

### MAS-DNP efficiency and reproducibility of measurements

The MAS-DNP efficiency of **AsymPol-TEK** and **cAsymPol-TEK** was investigated and compared to **TEKPol**. Hexagonal boron nitride (h-BN) was added to the solution to improve the microwave penetration and the DNP efficiency in TCE.[68]

To maximize the DNP enhancement, the nuclear spin–lattice relaxation should be slower than the rate at which the hyperpolarization is transferred throughout the system. This must be true for both the protons that are close to the radicals and also for the bulk ones.[21] In practice, it is possible to control to some extent the nuclear relaxation time for the bulk nuclei, $T_{1,n}^{\mathrm{Bulk}}$. For example, it can be lengthened by sample degassing that removes paramagnetic $O_2$ from the solution.[68,99] *In situ* freeze–thaw cycles, *via* sample insert/eject at 100 K under $N_2$, has been shown to be an efficient way to remove dissolved $O_2$ in TCE.[21,60] Nevertheless, reproducibility is sometimes poor when using TCE.[68] The main reason for this stems from the difficulty of forming a good glass in a reproducible manner, as indicated by the resulting $^{13}$C NMR linewidth.[68] This prevents the sample formulation from being easily optimised and makes it more difficult to assess the comparative performance of polarizing agents.

TCE can form several phases upon cooling, an amorphous glass phase, and three crystalline phases (denoted $\alpha$, $\beta$ and $\gamma$) that can be obtained between 100 and 170 K.[100] The metastable crystalline γ-phase can be formed upon heating the glass phase to 140–150 K.[100] This is illustrated in Fig. 4a and b, where the evolution of the $^{13}$C CPMAS NMR spectrum as a function of the sample temperature is shown for both **AsymPol-TEK** and **TEKPol**. In these experiments, after a cold insertion, the temperature of the sample was gradually increased from 120 to 160 K. The TCE glass phase is preserved until 130 K, giving rise to a single broad resonance in the $^{13}$C spectrum. The glass phase gradually converts into a crystalline phase in the 140–160 K range. This can be clearly seen with the appearance of resolved shoulders in the $^{13}$C TCE spectrum, corresponding to the dipolar coupling between the $^{13}$C and the $^{35}$Cl/$^{37}$Cl nuclei. We believe that we might be forming the metastable γ-phase, recently reported in the literature.[100] Upon cooling the sample back from 160 to 110 K, it results in the formation of the thermodynamically stable crystalline β-phase,[99] and inevitably gives rise to a reduction in DNP performance (as compared to the glass phase at the same temperature).[68]

To reproducibly obtain amorphous glass for TCE, we modified our experimental protocol (see Material and methods) to minimize the stator temperature at sample insertion. This implies flushing cold nitrogen gas inside the empty stator and

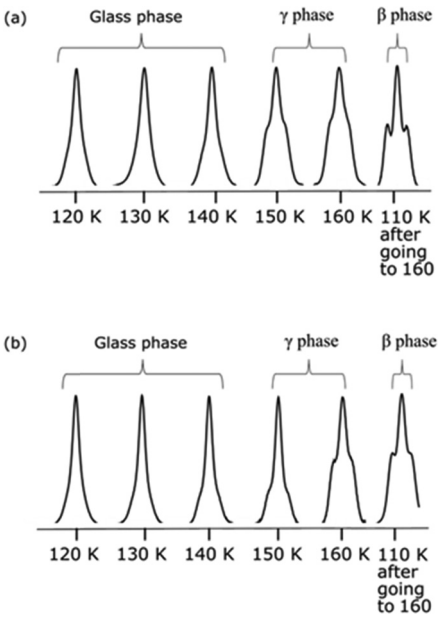


Fig. 4 $^{13}$C CP-MAS spectra (9.4 T) of 16 mM radical solutions of (a) **AsymPol-TEK** and (b) **TEKPol** in TCE in the presence of h-BN, as a function of the temperature. For better comparison of the lineshapes, all spectra are scaled to the same intensity. The last spectrum was obtained after slowly cooling back the sample from 160 K to 110 K.

 

turning off the μw irradiation before insertion. This protocol ensures a consistent glass formation, as shown for the $^{13}$C CPMAS TCE spectra at 9.4 T (for 16 mM **TEKPol**, **AsymPol-TEK** and **cAsymPol-TEK**) during the freeze–thaw cycles procedure (Fig. 5). All spectra correspond to the formation of a glass (no crystalline phase observed at any point in the cycle). This modified protocol significantly improves the reproducibility of the DNP measurement with TCE.

The effect of the oxygen removal on the $^{1}$H TCE $T_{1,n}^{\mathrm{Bulk}}$ can be seen in Fig. 6d. For this undoped TCE sample, $^{1}$H $T_{1,n}^{\mathrm{Bulk}}$ increases from ∼2.5 s, measured after the first freezing of the solution, to ∼70 s after 7 freeze–thaw cycles. The sensitivity at 9.4 T for each biradical as a function of the number of freeze–thaw cycles is given Fig. 6a. Over the course of 6 insert-ejects, the sensitivity increases moderately for all biradicals. **cAsymPol-TEK** provides a higher sensitivity (normalized to one) than **AsymPol-TEK** (0.8), while **TEKPol** is less sensitive (0.6–0.7). This behaviour is in sharp contrast with the corresponding DNP enhancement, $\epsilon_{\mathrm{on/off}}$ (Fig. 6c), which for **TEKPol**, increases from 140 to 307 between the first and the sixth freeze–thaw cycle. In contrast, $\epsilon_{\mathrm{on/off}}$ of **AsymPol-TEK** and **cAsymPol-TEK** varies much less, starting at ∼60 to end at 75 and 87, respectively, after 6 cycles. The stronger change in $\epsilon_{\mathrm{on/off}}$ for **TEKPol** is in part due to increased depolarization due to the lengthening of $^{1}$H bulk $T_1$, as seen through the decrease in signal intensity in the absence of microwave irradiation (Fig. 5). This effect is not present for the **AsymPol-TEK** PAs.

The stronger dependence of $\epsilon_{\mathrm{on/off}}$ on the number of freeze–thaw cycles for **TEKPol** may also come from its longer DNP build-up time, $T_{\mathrm{B}}$, compared to the **AsymPol-TEKs**. Interestingly, as seen in Fig. 6b, values of $T_{\mathrm{B}}$ are quite stable for the **AsymPol-TEK** radicals, with $T_{\mathrm{B}} \approx 1$ s for **AsymPol-TEK** and 0.5 s for **cAsymPol-TEK** at 9.4 T, while they are clearly increasing for **TEKPol** from 1.9 to 2.6 s over 6 freeze–thaw cycles. This suggests that the polarization build-up of the **AsymPol-TEK** PAs is less sensitive to the lengthening of $T_{1,n}^{\mathrm{Bulk}}$ than that of **TEKPol**.

Overall, the results reported here for **TEKPol** are consistent with previous reports,[60,66,72] keeping in mind that $\epsilon_{\mathrm{on/off}}$ factors do not correlate directly with NMR sensitivity. Similar experiments were also conducted at 14.1 T. The DNP performance of the three PAs is summarized in Table 2, at both 9.4 and 14.1 T. For this comparison, the reported values of $\varepsilon_{\mathrm{on/off}}$ and $T_{\mathrm{B}}$ correspond to the best sensitivity among each freeze–thaw series. At 14.1 T, **TEKPol** at 10 mM leads to $\epsilon_{\mathrm{on/off}} = 122$ and $T_{\mathrm{B}}$ = 9.1 s, and at 16 mM $\epsilon_{\mathrm{on/off}} = 128$ and $T_{\mathrm{B}}$ = 6.3 s after 6 freeze thaw cycles but also leads to significant depolarization with $\epsilon_{\mathrm{depo}} \sim 0.6$ (at 10 mM). **AsymPol-TEK** and **cAsymPol-TEK** at 10 mM led to lower $\epsilon_{\mathrm{on/off}}$, 74 and 80 respectively but with a

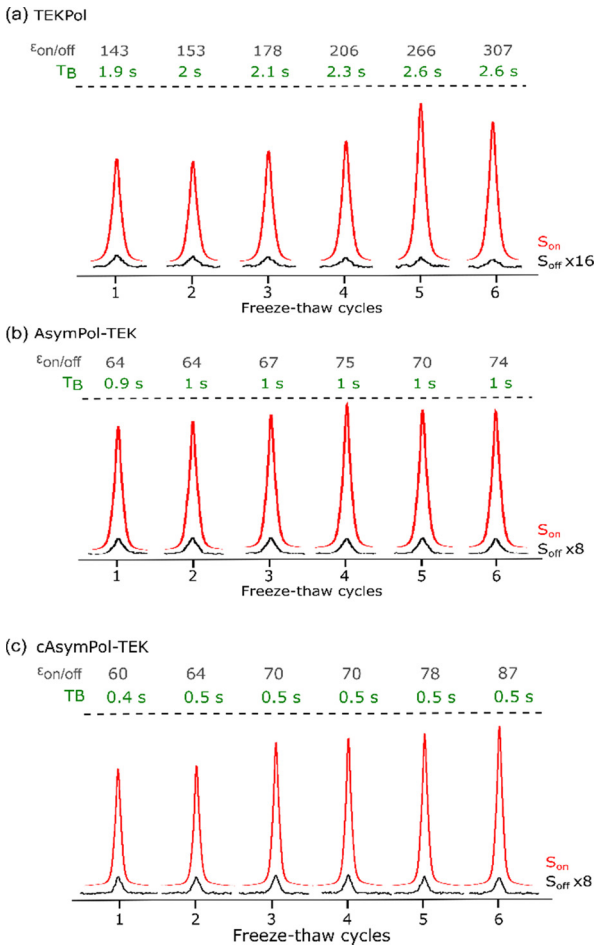


Fig. 5 $^{13}$C CP-MAS spectra of 16 mM radical solution of (a) **TEKPol**, (b) **AsymPol-TEK**, and (c) **cAsymPol-TEK** in TCE mixed with h-BN, as a function of the number of freeze–thaw cycles with (red) and without (black) μw irradiation, using a 3.2 mm rotor at 9.4 T, 8 kHz MAS frequency and 105 K. The $^{13}$C CP-MAS spectra were acquired with a recycle delay of 1.3·$T_{\mathrm{B}}$. The evolution of the normalized sensitivity, the build-up time $T_{\mathrm{B}}$, and $\epsilon_{\mathrm{on/off}}$ as a function of the number of freeze–thaw cycles can be compared for the 3 radicals in Fig. 6.

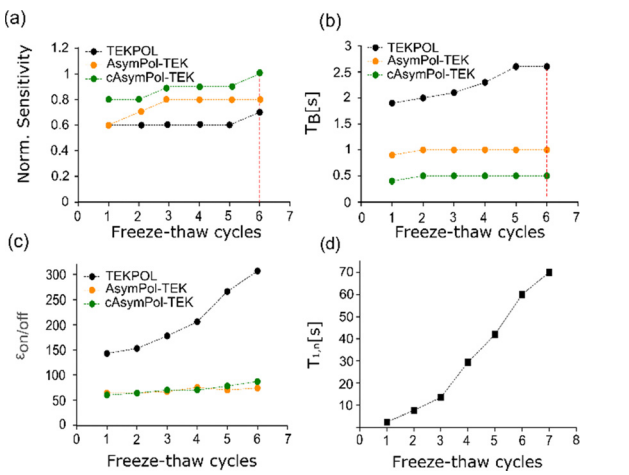


Fig. 6 (a) Normalized sensitivity $\left(S_{\mathrm{on}}/\sqrt{T_{\mathrm{B}}}\right)$, (b) build-up time $T_{\mathrm{B}}$ and (c) $\epsilon_{\mathrm{on/off}}$ values for 16 mM **TEKPol** (black), **AsymPol-TEK** (orange), and **cAsymPol-TEK** (green) in TCE mixed with h-BN, as a function of the number of freeze–thaw cycles. (d) Evolution of the proton longitudinal relaxation time $T_{1,n}$ for pure TCE (no radicals) as a function of the number of freeze–thaw cycles. All experiments were performed using a 3.2 mm rotor at 9.4 T, 8 kHz MAS frequency and 105 K.

Table 2 Experimental and simulated DNP performance of **TEKPol**, **AsymPol-TEK** and **cAsymPol-TEK** in TCE mixed with h-BN, at 9.4 T (16 mM) and 14.1 T (10 and 16 mM), and 8 kHz MAS

| | $T_B$[s][b] | $\varepsilon_{on/off}$ [b] | Sensitivity[a] |
|---|---|---|---|
| 9.4 T | | | |
| **TEKPol** (16 mM) (exp/**sim**) | 2.6/**3.2** | 307/**300** | 0.7 |
| **AsymPol-TEK** (16 mM) (exp/**sim**) | 1/**0.7** | 75/**115** | 0.8 |
| **cAsymPol-TEK** (16 mM) (exp/**sim**) | 0.5/**0.7** | 87/**136** | 1 |
| 14.1 T | | | |
| **TEKPol** (10 mM) (exp/**sim**) | 9.1/**7.6** | 122/**128** | 0.4 |
| **TEKPol** (16 mM) (exp/**sim**) | 6.3/**4.8** | 128/**165** | 0.45 |
| **AsymPol-TEK** (10 mM) (exp/**sim**) | 2.3/**1.8** | 74/**73** | 0.7 |
| **cAsymPol-TEK** (10 mM) (exp/**sim**) | 1.8/**2** | 80/**89** | 1 |

[a] The sensitivity is normalized to the highest value. [b] Light numbers are experimental values. Outcome of MAS-DNP simulations are in bold.

much shorter $T_B \approx 2$ s. Once the depolarization has been accounted for ($\epsilon_{depo} \sim 0.75$ for both **AsymPol-TEKs**), **AsymPol-TEK** and **cAsymPol-TEK** yield 1.75- and 2.5-times higher sensitivity than **TEKPol**, respectively. All in all, the **AsymPol-TEK** PAs clearly yield higher sensitivity than **TEKPol** at both fields, with a more pronounced improvement for the methyl-free **cAsymPol-TEK** and at the higher magnetic field. We note here that the polarization build-up curve of **AsymPol-TEK** in presence of μw is not purely mono-exponential, but slightly bi- or stretched exponential.

The experimental performance of the different radicals was compared to MAS-DNP simulations (Table 2). For all PAs, the build-up times are relatively well reproduced by simulations at both magnetic fields. The DNP enhancement for **TEKPol** is also well reproduced for 16 mM concentration at 9.4 T and 10 mM at 14.1 T but it is overestimated for 16 mM at 14.1 T. The concentration trend at 14.1 T is consistent, with the simulations predicting that 10 mM **TEKPol** yields a slower build-up time than 16 mM. This confirms the robustness of the model used for the simulations. For **AsymPol-TEK** and **cAsymPol-TEK**, the predicted values of $T_B$ are very close to the experimental data at both fields, whereas the DNP enhancements are slightly overestimated at 9.4 T but well reproduced at 14.1 T. A better agreement between simulations and experiment could be obtained by adjusting the electron and nuclear relaxation times. However, we preferred to keep the same nuclear relaxation times for all PAs (both for the protons close to the biradicals and for the bulk ones). This highlights the origin of the fast build-up times of the **AsymPol-TEK** radicals, namely the stronger e–e couplings (dipolar and *J*-exchange interaction) compared to **TEKPol**, in line with the results reported for the water-soluble members the AsymPol family.[45,49]

The improved DNP sensitivity yielded by both **AsymPol-TEK** and **cAsymPol-TEK** is directly related to the shorter build-up time $T_B$, as compared to **TEKPol**. The higher values of $\varepsilon_{on/off}$ obtained with **TEKPol** (Fig. 6c) are related to its stronger depolarization, with $\varepsilon_{depo}$ around 0.5 both at 9.4 and 14.1 T at 16 mM concentration (see Table S2, ESI†), which led to a significant overestimation of the hyperpolarization gain. The situation is very different for the **AsymPol-TEKs**, that exhibit a smaller depolarization effect ($\varepsilon_{depo}$ = 0.9–0.8 at 16 mM and 9.4 T; 0.75 at 10 mM and 14.1 T), which is another important characteristic of the AsymPol PAs.[45,49]

## Open and close biradicals

So far, all the experiments reported for **AsymPol-TEK** were performed with isomer A, where phenyl groups are in an equatorial position with an "open–open" conformation. However, changing the configuration at the carbons connected to the phenyl groups can give two other stereoisomers, shown in Fig. 7. A ring flip of the cyclohexyl ring will place the phenyl group in the more accommodating equatorial group and move the cyclohexyl closer to the nitroxide, giving a "closed" conformation. Thus, the two isomers, other than isomer A, that are possible will adopt either an "open–close" or a "close–close" structure. Although we were not able to crystallise isomer B, we assume that it corresponds to the "open–closed" isomer as it is lower in energy than the "closed–closed" structure.

The MAS-DNP performance of the **AsymPol-TEK** "open–close" isomer B (Fig. 7) was found to be far inferior to the "open–open" isomer A, with $\epsilon_{on/off} \approx 33$ and $T_B = 0.4$ s at 9.4 T and $\epsilon_{on/off} \approx 32$ and $T_B = 1.9$ s at 14.1 T. DFT simulations of isomer B yielded two conformers with unfavourable relative orientation of the *g*-tensors ($L_{a,b} = 4.7 \times 10^{-3}$). Moreover, the predicted exchange interaction is larger ($J_{a,b} \approx 140$ MHz). Both characteristics, unfavourable *g*-tensor relative orientation and too strong exchange interaction, explain the poor DNP performance of isomer B.

The "closed–closed" conformation, even though not obtained in the synthesis, can also be explored in-silico. The relative "distance" of the *g*-tensors is higher ($L_{a,b} = 5.8 \times 10^{-3}$), equivalent to the (better) conformer **#2** of isomer A. However, the predicted exchange interaction is significantly higher with $J_{a,b} \approx 250$ MHz. This would make MAS-DNP very inefficient at lower fields, as $|2J_{a,b}| > \nu_n$, but could potentially be of interest at higher fields.

## Applications

The efficiency of the **AsymPol-TEKs** was tested by hyperpolarizing proton-dense microcrystals of adenosine and caffeine at 9.4 T and 105 K (see Table S3, ESI†). Overall, **cAsymPol-TEK**

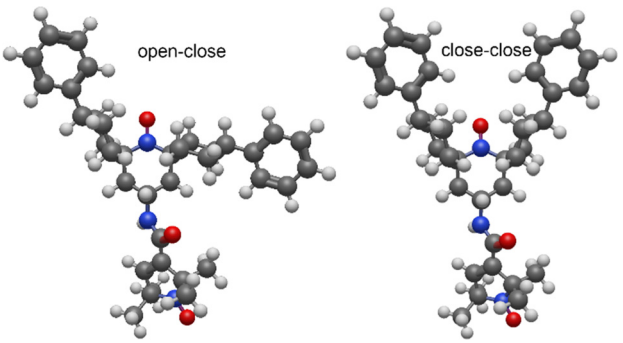


Fig. 7 3D structures of the open–closed (left) and closed–closed (right) isomers of **AsymPol-TEK**.

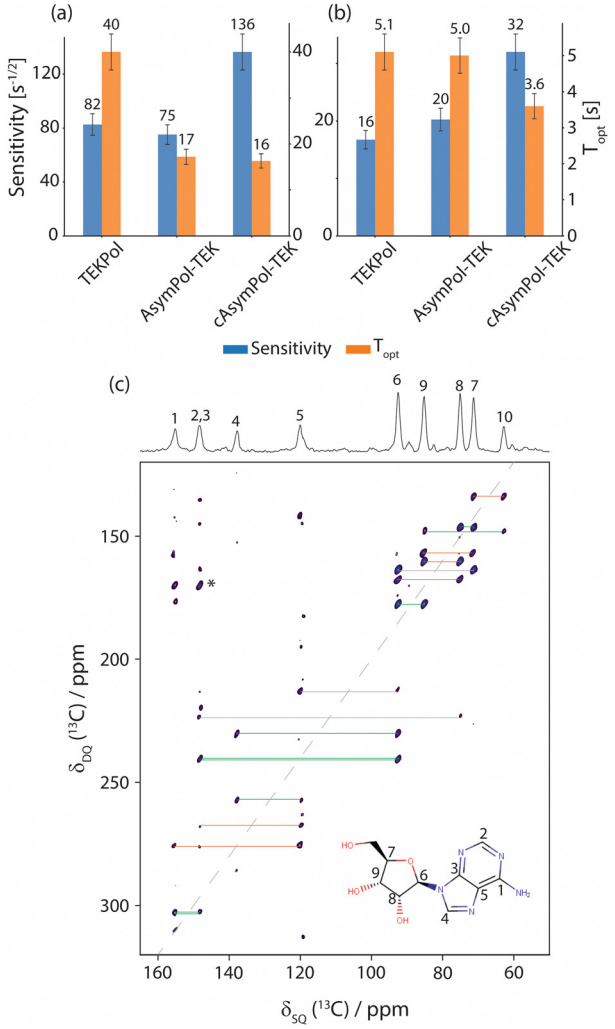


Fig. 8 (a) and (b) Signal-to-noise ratio per square root of the experimental time (in blue) and optimal recycle delay $T_{opt}$ (in orange) of (a) adenosine and (b) caffeine powders impregnated with 10 mM **TEKPol**, **AsymPol-TEK** and **cAsymPol-TEK** in TCE. (c) DNP-enhanced 2D $^{13}C$–$^{13}C$ DQ-SQ correlation spectra of adenosine microcrystals at NA using **cAsymPol-TEK**. The experiment was acquired using SR26 as dipolar recoupling sequence, at 6.6 kHz MAS, 105 K and 9.4 T. Experimental time was 10 h and the total mixing time for SR26 was 4.8 ms. $^{13}C$–$^{13}C$ correlations are mapped out on the 2D spectra, in orange for one-bond correlations, green for two-bonds, and grey for ≥ three-bonds. Spinning side bands are indicated with asterisks. The chemical structure of adenosine with numbering of the carbon atoms is given as inset.

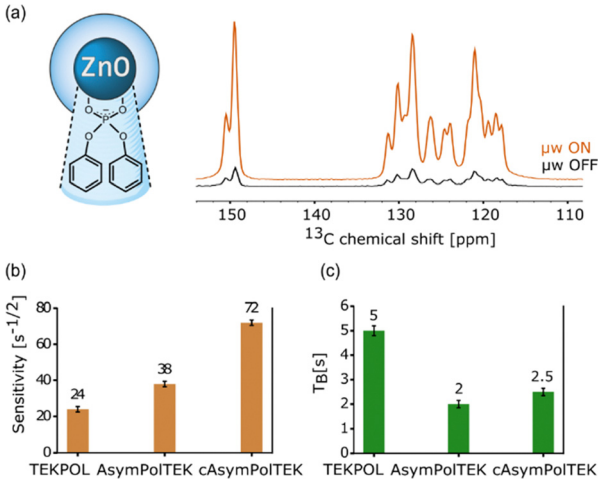


Fig. 9 (a) {$^1H$-}$^{13}C$ CPMAS spectra of ZnO-DPP NCs impregnated with 10 mM cAsymPol-TEK in TCE with (orange) and without (black) μw irradiation. (b) Sensitivity and (c) proton $T_B$ of ZnO-DPP NCs impregnated with 10 mM **TEKPol**, **AsymPol-TEK** and **cAsymPol-TEK** in TCE. $\varepsilon_{on/off}$ values were 9 for **TEKPol**, 6 for **AsymPol-TEK**, and 10 for **cAsymPol-TEK**. All data were recorded at 9.4 T, 8 kHz MAS frequency and 105 K.

yields a higher sensitivity (signal-to-noise ratio per square root of time) compared to **AsymPol-TEK** and **TEKPol**, both for adenosine and caffeine microcrystals (Fig. 8a and b). As expected, the sensitivity under microwave irradiation is higher for adenosine than caffeine microcrystals owing to the shorter $^1H$ bulk $T_{1,n}$ of the latter. Note that we did not optimize the radical or solvent proton concentration here.[49] Using a biradical concentration of 10 mM, **cAsymPol-TEK** provides about x2.5 to x4 improvement in time-savings for adenosine and caffeine microcrystals respectively. This allows recording DQ/SQ $^{13}C$–$^{13}C$ correlation experiments at natural isotopic abundance in a few hours using **cAsymPol-TEK**. Fig. 8c shows a 2D experiment with high S/N recorded in 10 h on adenosine microcrystals. Thanks to the mixing time chosen, one can clearly detect polarization transfer corresponding to carbon spins distant by one, two and three-bond. Fig. S2 (ESI†) shows that in the more challenging case of caffeine, it is possible to get clear cross-peaks in about one hour of experimental time. A third example of DQ/SQ $^{13}C$–$^{13}C$ correlation experiments at the higher magnetic field of 14.1 T on histidine at natural isotopic abundance using **AsymPol-TEK** can be found in Fig. S3 (ESI†).

Finally, we also used **TEKPol**, **AsymPol-TEK** and **cAsymPol-TEK** to polarize the surface of semiconducting nanocrystals. More specifically, we chose ZnO nanocrystals coated by mono-anionic diphenyl phosphate (DPP) ligands, that were synthetized using an one-pot self-supporting organometallic (OSSOM) approach.[101,102] Details of the synthesis can be found in the ESI.† Fig. 9 shows the NMR sensitivity and the proton build-up time $T_B$ for the ZnO NCs impregnated with TCE. The **AsymPol-TEKs** yield an improvement in sensitivity over **TEKPol**, which translates into a x9 in time-saving for **cAsymPol-TEK**. These results open interesting prospects for the study of challenging materials (bulk and surface) by MAS-DNP.

## Conclusions

In summary, we have introduced two new members of the AsymPol family for non-aqueous applications, named **AsymPol-TEK** and **cAsymPol-TEK**. Both PAs provide improved sensitivity compared to **TEKPol** at both 9.4 and 14.1 T. By ensuring that the TCE-based DNP sample is always introduced into a probe head with a temperature around 100 K or below, the reproducibility of the DNP measurements with TCE can be significantly improved. The efficiency of these PAs can be rationalized using a combination of DFT, MD, EPR and MAS-DNP simulations that

reveal the presence of two major conformers. In addition, these results show that the introduction of the spirocyclohexyl groups does not significantly change the linker geometry, nor the e–e spin couplings involved. Thus, the improved performance of **cAsymPol-TEK** relative to **AsymPol-TEK** is attributed to the replacement of methyl groups with cyclohexyl groups, which tends to lengthen both the electron and the core protons relaxation times, leading to better CE-DNP efficiency.

The key advantage of the **AsymPol-TEK** PAs lies not only in their high polarization gain but also in their fast hyperpolarization build-up times. This makes them ideal to polarize proton-dense systems, and/or systems with short intrinsic $^{1}$H nuclear relaxation times. This is illustrated with the acquisition of $^{13}$C–$^{13}$C correlation experiments at natural isotopic abundance of organic microcrystals, and to polarize ligands at the surface of ZnO nanocrystals.

## Conflicts of interest

There are no conflicts to declare.

## Acknowledgements

This work was supported by the French National Research Agency (CBH-EUR-GS and Labex ARCANE ANR-17-EURE-0003, Glyco@Alps ANR-15-IDEX-02) and the European Research Council Grant ERC-CoG-2015 No. 682895 to G. D. P. Part of this work, carried out on the Platform for Nanocharacterisation (PFNC), was supported by the ''Recherches Technologiques de Base'' program of the French National Research Agency (ANR). This work was supported by the Icelandic Research Fund, grant No. 239662, the University of Iceland Research Fund (S. Th. S) and a doctoral fellowship from the University of Iceland Research Fund (SC). T.H. thanks the Deutsche Forschungsgemeinschaft (DFG) for a postdoctoral fellowship (414196920). F. M. V. thanks Carl Fleischer for the histidine sample. The National High Magnetic Field Laboratory is supported by the NSF (DMR-1644779 and DMR-2128556) and by the State of Florida. The 14.1 T MAS-DNP system at NHMFL is funded in part by NIH S10 OD018519 (magnet and console), NIH P41 GM122698 and RM1-GM148766, and EU H2020-INFRAIA Grant No. 101008500.

## References

1 Q. Z. Ni, E. Daviso, T. V. Can, E. Markhasin, S. K. Jawla, T. M. Swager, R. J. Temkin, J. Herzfeld and R. G. Griffin, High Frequency Dynamic Nuclear Polarization, *Acc. Chem. Res.*, 2013, **46**, 1933–1941.

2 A. S. Lilly Thankamony, J. J. Wittmann, M. Kaushik and B. Corzilius, Dynamic nuclear polarization for sensitivity enhancement in modern solid-state NMR, *Prog. Nucl. Magn. Reson. Spectrosc.*, 2017, **102–103**, 120–195.

3 S. Hediger, D. Lee, F. Mentink-Vigier and G. De Paëpe, *eMagRes*, John Wiley & Sons, Ltd, 2018, pp. 105–116.

4 A. B. Barnes, G. De Paëpe, P. C. A. van der Wel, K.-N. Hu, C.-G. Joo, V. S. Bajaj, M. L. Mak-Jurkauskas, J. R. Sirigiri, J. Herzfeld, R. J. Temkin and R. G. Griffin, High-Field Dynamic Nuclear Polarization for Solid and Solution Biological NMR, *Appl. Magn. Reson.*, 2008, **34**, 237–263.

5 K. Kundu, F. Mentink-Vigier, A. Feintuch and S. Vega, *eMagRes*, John Wiley & Sons, Ltd, 2019, pp. 295–338.

6 T. V. Can, Q. Z. Ni and R. G. Griffin, Mechanisms of dynamic nuclear polarization in insulating solids, *J. Magn. Reson.*, 2015, **253**, 23–35.

7 K.-N. Hu, H. Yu, T. M. Swager and R. G. Griffin, Dynamic Nuclear Polarization with Biradicals, *J. Am. Chem. Soc.*, 2004, **126**, 10844–10845.

8 C. Song, K. N. Hu, C. G. Joo, T. M. Swager and R. G. Griffin, TOTAPOL: A biradical polarizing agent for dynamic nuclear polarization experiments in aqueous media, *J. Am. Chem. Soc.*, 2006, **128**, 11385–11390.

9 K. Jaudzems, T. Polenova, G. Pintacuda, H. Oschkinat and A. Lesage, DNP NMR of biomolecular assemblies, *J. Struct. Biol.*, 2019, **206**, 90–98.

10 A. J. Rossini, C. M. Widdifield, A. Zagdoun, M. Lelli, M. Schwarzwälder, C. Copéret, A. Lesage and L. Emsley, Dynamic nuclear polarization enhanced NMR spectroscopy for pharmaceutical formulations, *J. Am. Chem. Soc.*, 2014, **136**, 2324–2334.

11 D. Gauto, O. Dakhlaoui, I. Marin-Montesinos, S. Hediger and G. D. Paëpe, Targeted DNP for biomolecular solid-state NMR, *Chem. Sci.*, 2021, **12**, 6223–6237.

12 B. Plainchont, P. Berruyer, J.-N. Dumez, S. Jannin and P. Giraudeau, Dynamic Nuclear Polarization Opens New Perspectives for NMR Spectroscopy in Analytical Chemistry, *Anal. Chem.*, 2018, **90**, 3639–3650.

13 W. Y. Chow, G. De Paëpe and S. Hediger, Biomolecular and Biological Applications of Solid-State NMR with Dynamic Nuclear Polarization Enhancement, *Chem. Rev.*, 2022, **122**, 9795–9847.

14 N. Ghassemi, A. Poulhazan, F. Deligey, F. Mentink-Vigier, I. Marcotte and T. Wang, Solid-State NMR Investigations of Extracellular Matrixes and Cell Walls of Algae, Bacteria, Fungi, and Plants, *Chem. Rev.*, 2022, **122**, 10036–10086.

15 T. Biedenbänder, V. Aladin, S. Saeidpour and B. Corzilius, Dynamic Nuclear Polarization for Sensitivity Enhancement in Biomolecular Solid-State NMR, *Chem. Rev.*, 2022, **122**, 9738–9794.

16 A. J. Rossini, A. Zagdoun, M. Lelli, A. Lesage, C. Cop, L. Emsley, C. Copéret and L. Emsley, Dynamic Nuclear Polarization Surface Enhanced NMR Spectroscopy, *Acc. Chem. Res.*, 2013, **46**, 1942–1951.

17 D. Lee, S. Hediger and G. De Paepe, Is solid-state NMR enhanced by dynamic nuclear polarization?, *Solid State Nucl. Magn. Reson.*, 2015, **66–67**, 6–20.

18 F. A. Perras, T. Kobayashi and M. Pruski, Growing signals from the noise: Challenging nuclei in materials DNP, *eMagRes*, 2018, **7**, 35–50.

19 A. G. M. Rankin, J. Trébosc, F. Pourpoint, J. P. Amoureux and O. Lafon, Recent developments in MAS DNP-NMR of

materials, *Solid State Nucl. Magn. Reson.*, 2019, **101**, 116–143.

20 Ü. Akbey, W. T. Franks, A. Linden, M. Orwick-Rydmark, S. Lange and H. Oschkinat, in *Hyperpolarization Methods in NMR Spectroscopy*, ed. L. T. Kuhn, Springer Berlin Heidelberg, Berlin, Heidelberg, 2013, vol. 338, pp. 181–228.

21 B. Corzilius, L. B. Andreas, A. A. Smith, Q. Z. Ni and R. G. Griffin, Paramagnet induced signal quenching in MAS–DNP experiments in frozen homogeneous solutions, *J. Magn. Reson.*, 2014, **240**, 113–123.

22 H. Takahashi, C. Fernández-de-Alba, D. Lee, V. Maurel, S. Gambarelli, M. Bardet, S. Hediger, A.-L. Barra and G. De Paëpe, Optimization of an absolute sensitivity in a glassy matrix during DNP-enhanced multidimensional solid-state NMR experiments, *J. Magn. Reson.*, 2014, **239**, 91–99.

23 T. Kobayashi, O. Lafon, A. S. Lilly Thankamony, I. I. Slowing, K. Kandel, D. Carnevale, V. Vitzthum, H. Vezin, J.-P. Amoureux, G. Bodenhausen and M. Pruski, Analysis of sensitivity enhancement by dynamic nuclear polarization in solid-state NMR: a case study of functionalized mesoporous materials, *Phys. Chem. Chem. Phys.*, 2013, **15**, 5553.

24 A. J. Rossini, A. Zagdoun, M. Lelli, D. Gajan, F. Rascón, M. Rosay, W. E. Maas, C. Copéret, A. Lesage and L. Emsley, One hundred fold overall sensitivity enhancements for Silicon-29 NMR spectroscopy of surfaces by dynamic nuclear polarization with CPMG acquisition, *Chem. Sci.*, 2012, **3**, 108–115.

25 K. R. Thurber and R. Tycko, Theory for cross effect dynamic nuclear polarization under magic-angle spinning in solid state nuclear magnetic resonance: The importance of level crossings, *J. Chem. Phys.*, 2012, **137**, 084508.

26 F. Mentink-Vigier, U. Akbey, Y. Hovav, S. Vega, H. Oschkinat and A. Feintuch, Fast passage dynamic nuclear polarization on rotating solids, *J. Magn. Reson.*, 2012, **224**, 13–21.

27 F. Mentink-Vigier, Ü. Akbey, H. Oschkinat, S. Vega and A. Feintuch, Theoretical aspects of Magic Angle Spinning - Dynamic Nuclear Polarization, *J. Magn. Reson.*, 2015, **258**, 102–120.

28 F. Mentink-Vigier, S. Vega and G. De Paëpe, Fast and accurate MAS–DNP simulations of large spin ensembles, *Phys. Chem. Chem. Phys.*, 2017, **19**, 3506–3522.

29 F. Mentink-Vigier, Optimizing nitroxide biradicals for cross-effect MAS-DNP: The role of: G -tensors' distance, *Phys. Chem. Chem. Phys.*, 2020, **22**, 3643–3652.

30 F. Mentink-Vigier, A.-L. Barra, J. van Tol, S. Hediger, D. Lee and G. De Paëpe, *De novo* prediction of cross-effect efficiency for magic angle spinning dynamic nuclear polarization, *Phys. Chem. Chem. Phys.*, 2019, **21**, 2166–2176.

31 K. R. Thurber and R. Tycko, Perturbation of nuclear spin polarizations in solid state NMR of nitroxide-doped samples by magic-angle spinning without microwaves, *J. Chem. Phys.*, 2014, **140**, 184201.

32 A. Equbal, A. Leavesley, S. K. Jain and S. Han, Cross-Effect Dynamic Nuclear Polarization Explained: Polarization, Depolarization, and Oversaturation, *J. Phys. Chem. Lett.*, 2019, **10**, 548–558.

33 F. Mentink-Vigier, T. Dubroca, J. Van Tol and S. T. Sigurdsson, The distance between g-tensors of nitroxide biradicals governs MAS-DNP performance: The case of the bTurea family, *J. Magn. Reson.*, 2021, **329**, 107026.

34 F. Mentink-Vigier, S. Paul, D. Lee, A. Feintuch, S. Hediger, S. Vega and G. De Paëpe, Nuclear depolarization and absolute sensitivity in magic-angle spinning cross effect dynamic nuclear polarization, *Phys. Chem. Chem. Phys.*, 2015, **17**, 21824–21836.

35 M. Rosay, L. Tometich, S. Pawsey, R. Bader, R. Schauwecker, M. Blank, P. M. Borchard, S. R. Cauffman, K. L. Felch, R. T. Weber, R. J. Temkin, R. G. Griffin and W. E. Maas, Solid-state dynamic nuclear polarization at 263 GHz: spectrometer design and experimental results, *Phys. Chem. Chem. Phys.*, 2010, **12**, 5850.

36 M. Rosay, M. Blank and F. Engelke, Instrumentation for solid-state dynamic nuclear polarization with magic angle spinning NMR, *J. Magn. Reson.*, 2016, **264**, 88–98.

37 E. Bouleau, P. Saint-Bonnet, F. Mentink-Vigier, H. Takahashi, J.-F. Jacquot, M. Bardet, F. Aussenac, A. Purea, F. Engelke, S. Hediger, D. Lee and G. De Paëpe, Pushing NMR sensitivity limits using dynamic nuclear polarization with closed-loop cryogenic helium sample spinning, *Chem. Sci.*, 2015, **6**, 6806–6812.

38 Y. Matsuki, K. Ueda, T. Idehara, R. Ikeda, I. Ogawa, S. Nakamura, M. Toda, T. Anai and T. Fujiwara, Helium-cooling and -spinning dynamic nuclear polarization for sensitivity-enhanced solid-state NMR at 14 T and 30 K, *J. Magn. Reson.*, 2012, **225**, 1–9.

39 D. Lee, E. Bouleau, P. Saint-Bonnet, S. Hediger and G. De Paëpe, Ultra-low temperature MAS-DNP, *J. Magn. Reson.*, 2016, **264**, 116–124.

40 Y. Matsuki, S. Nakamura, S. Fukui, H. Suematsu and T. Fujiwara, Closed-cycle cold helium magic-angle spinning for sensitivity-enhanced multi-dimensional solid-state NMR, *J. Magn. Reson.*, 2015, **259**, 76–81.

41 K. R. Thurber, A. Potapov, W.-M. Yau and R. Tycko, Solid state nuclear magnetic resonance with magic-angle spinning and dynamic nuclear polarization below 25 K, *J. Magn. Reson.*, 2012, **226**, 100–106.

42 K. Thurber and R. Tycko, Low-temperature dynamic nuclear polarization with helium-cooled samples and nitrogen-driven magic-angle spinning, *J. Magn. Reson.*, 2016, **264**, 99–106.

43 D. A. Hall, D. C. Maus, G. J. Gerfen, S. J. Inati, L. R. Becerra, F. W. Dahlquist and R. G. Griffin, Polarization-Enhanced NMR Spectroscopy of Biomolecules in Frozen Solution, *Science*, 1997, **276**, 930–932.

44 Y. Matsuki, S. Nakamura, F. Hobo, Y. Endo, H. Takahashi, H. Suematsu and T. Fujiwara, Cryogenic signal amplification combined with helium-temperature MAS DNP toward ultimate NMR sensitivity at high field conditions, *J. Magn. Reson.*, 2022, **335**, 107139.

45 F. Mentink-Vigier, I. Marin-Montesinos, A. P. Jagtap, T. Halbritter, J. van Tol, S. Hediger, D. Lee, S. T. Sigurdsson

and G. De Paëpe, Computationally Assisted Design of Polarizing Agents for Dynamic Nuclear Polarization Enhanced NMR: The AsymPol Family, *J. Am. Chem. Soc.*, 2018, **140**, 11013–11019.

46 A. Lund, G. Casano, G. Menzildjian, M. Kaushik, G. Stevanato, M. Yulikov, R. Jabbour, D. Wisser, M. Renom-Carrasco, C. Thieuleux, F. Bernada, H. Karoui, D. Siri, M. Rosay, I. V. Sergeyev, D. Gajan, M. Lelli, L. Emsley, O. Ouari and A. Lesage, TinyPols: A family of water-soluble binitroxides tailored for dynamic nuclear polarization enhanced NMR spectroscopy at 18.8 and 21.1 T, *Chem. Sci.*, 2020, **11**, 2810–2818.

47 C. Sauvée, M. Rosay, G. Casano, F. Aussenac, R. T. Weber, O. Ouari and P. Tordo, Highly efficient, water-soluble polarizing agents for dynamic nuclear polarization at high frequency, *Angew. Chem., Int. Ed.*, 2013, **52**, 10858–10861.

48 A. Zagdoun, G. Casano, O. Ouari, M. Schwarzwälder, A. J. Rossini, F. Aussenac, M. Yulikov, G. Jeschke, C. Copéret, A. Lesage, P. Tordo and L. Emsley, Large Molecular Weight Nitroxide Biradicals Providing Efficient Dynamic Nuclear Polarization at Temperatures up to 200 K, *J. Am. Chem. Soc.*, 2013, **135**, 12790–12797.

49 R. Harrabi, T. Halbritter, F. Aussenac, O. Dakhlaoui, J. van Tol, K. K. Damodaran, D. Lee, S. Paul, S. Hediger, F. Mentink-Vigier, S. T. Sigurdsson and G. De Paëpe, Highly Efficient Polarizing Agents for MAS-DNP of Proton-Dense Molecular Solids, *Angew. Chem., Int. Ed.*, 2022, **61**, e202114103.

50 G. Mathies, M. A. Caporini, V. K. Michaelis, Y. Liu, K.-N. Hu, D. Mance, J. L. Zweier, M. Rosay, M. Baldus and R. G. Griffin, Efficient Dynamic Nuclear Polarization at 800 MHz/527 GHz with Trityl-Nitroxide Biradicals, *Angew. Chem., Int. Ed.*, 2015, **54**, 11770–11774.

51 F. Mentink-Vigier, G. Mathies, Y. Liu, A.-L. A.-L. L. Barra, M. A. M. A. Caporini, D. Lee, S. Hediger, R. Griffin, G. De Paëpe, R. G. Griffin and G. De Paëpe, Efficient cross-effect dynamic nuclear polarization without depolarization in high-resolution MAS NMR, *Chem. Sci.*, 2017, **8**, 8150–8163.

52 W. Zhai, A. Lucini Paioni, X. Cai, S. Narasimhan, J. Medeiros-Silva, W. Zhang, A. Rockenbauer, M. Weingarth, Y. Song, M. Baldus and Y. Liu, Postmodification via Thiol-Click Chemistry Yields Hydrophilic Trityl-Nitroxide Biradicals for Biomolecular High-Field Dynamic Nuclear Polarization, *J. Phys. Chem. B*, 2020, **124**, 9047–9060.

53 X. Cai, A. Lucini Paioni, A. Adler, R. Yao, W. Zhang, D. Beriashvili, A. Safeer, A. Gurinov, A. Rockenbauer, Y. Song, M. Baldus and Y. Liu, Highly Efficient Trityl-Nitroxide Biradicals for Biomolecular High-Field Dynamic Nuclear Polarization, *Chem. – Eur. J.*, 2021, **27**, 12758–12762.

54 T. Halbritter, R. Harrabi, S. Paul, J. Van Tol, D. Lee, S. Hediger, S. T. Sigurdsson, F. Mentink-Vigier and G. De Paëpe, PyrroTriPol: a semi-rigid trityl-nitroxide for high field dynamic nuclear polarization, *Chem. Sci.*, 2023, **14**, 3852–3864.

55 R. Yao, D. Beriashvili, W. Zhang, S. Li, A. Safeer, A. Gurinov, A. Rockenbauer, Y. Yang, Y. Song, M. Baldus and Y. Liu, Highly bioresistant, hydrophilic and rigidly linked trityl-nitroxide biradicals for cellular high-field dynamic nuclear polarization, *Chem. Sci.*, 2022, **13**, 14157–14164.

56 D. Wisser, G. Karthikeyan, A. Lund, G. Casano, H. Karoui, M. Yulikov, G. Menzildjian, A. C. Pinon, A. Purea, F. Engelke, S. R. Chaudhari, D. Kubicki, A. J. Rossini, I. B. Moroz, D. Gajan, C. Copéret, G. Jeschke, M. Lelli, L. Emsley, A. Lesage and O. Ouari, BDPA-Nitroxide Biradicals Tailored for Efficient Dynamic Nuclear Polarization Enhanced Solid-State NMR at Magnetic Fields up to 21.1 T, *J. Am. Chem. Soc.*, 2018, **140**, 13340–13349.

57 P. Berruyer, S. Björgvinsdóttir, A. Bertarello, G. Stevanato, Y. Rao, G. Karthikeyan, G. Casano, O. Ouari, M. Lelli, C. Reiter, F. Engelke and L. Emsley, Dynamic Nuclear Polarization Enhancement of 200 at 21.15 T Enabled by 65 kHz Magic Angle Spinning, *J. Phys. Chem. Lett.*, 2020, **11**, 8386–8391.

58 A. Zagdoun, A. J. Rossini, D. Gajan, A. Bourdolle, O. Ouari, M. Rosay, W. E. Maas, P. Tordo, M. Lelli, L. Emsley, A. Lesage and C. Copéret, Non-aqueous solvents for DNP surface enhanced NMR spectroscopy, *Chem. Commun.*, 2012, **48**, 654–656.

59 Y. Matsuki, T. Maly, O. Ouari, H. Karoui, F. Le Moigne, E. Rizzato, S. Lyubenova, J. Herzfeld, T. Prisner, P. Tordo and R. G. Griffin, Dynamic Nuclear Polarization with a Rigid Biradical, *Angew. Chem., Int. Ed.*, 2009, **48**, 4996–5000.

60 D. J. Kubicki, G. Casano, M. Schwarzwälder, S. Abel, C. Sauvée, K. Ganesan, M. Yulikov, A. J. Rossini, G. Jeschke, C. Copéret, A. Lesage, P. Tordo, O. Ouari and L. Emsley, Rational design of dinitroxide biradicals for efficient cross-effect dynamic nuclear polarization, *Chem. Sci.*, 2015, **7**, 550–558.

61 A. Venkatesh, G. Casano, Y. Rao, F. De Biasi, F. A. Perras, D. J. Kubicki, D. Siri, S. Abel, H. Karoui, M. Yulikov, O. Ouari and L. Emsley, Deuterated TEKPol Biradicals and the Spin-Diffusion Barrier in MAS DNP, *Angew. Chem., Int. Ed.*, 2023, **62**, e202304844.

62 Y. Matsuki, T. Maly, O. Ouari, H. Karoui, F. Le Moigne, E. Rizzato, S. Lyubenova, J. Herzfeld, T. Prisner, P. Tordo and R. G. Griffin, Dynamic Nuclear Polarization with a Rigid Biradical, *Angew. Chem., Int. Ed.*, 2009, **48**, 4996–5000.

63 T. Maly, G. T. Debelouchina, V. S. Bajaj, K.-N. Hu, C.-G. Joo, M. L. Mak–Jurkauskas, J. R. Sirigiri, P. C. A. van der Wel, J. Herzfeld, R. J. Temkin and R. G. Griffin, Dynamic nuclear polarization at high magnetic fields, *J. Chem. Phys.*, 2008, **128**, 052211.

64 C. Presti, A. S. L. Thankamony, J. G. Alauzun, P. H. Mutin, D. Carnevale, C. Lion, H. Vezin, D. Laurencin and O. Lafon, NMR and EPR Characterization of Functionalized Nanodiamonds, *J. Phys. Chem. C*, 2015, **119**, 12408–12422.

65 H. Nagashima, J. Trébosc, Y. Kon, O. Lafon and J. Amoureux, Efficient transfer of DNP-enhanced $^{1}$H magnetization to half-integer quadrupolar nuclei in solids at moderate spinning rate, *Magn. Reson. Chem.*, 2021, **59**, 920–939.

66 M. P. Hanrahan, Y. Chen, R. Blome-Fernández, J. L. Stein, G. F. Pach, M. A. S. Adamson, N. R. Neale, B. M. Cossairt,

J. Vela and A. J. Rossini, Probing the Surface Structure of Semiconductor Nanoparticles by DNP SENS with Dielectric Support Materials, *J. Am. Chem. Soc.*, 2019, **141**, 15532–15546.

67 F. A. Perras, U. Chaudhary, I. I. Slowing and M. Pruski, Probing Surface Hydrogen Bonding and Dynamics by Natural Abundance, Multidimensional, $^{17}$ O DNP-NMR Spectroscopy, *J. Phys. Chem. C*, 2016, **120**, 11535–11544.

68 D. J. Kubicki, A. J. Rossini, A. Purea, A. Zagdoun, O. Ouari, P. Tordo, F. Engelke, A. Lesage and L. Emsley, Amplifying Dynamic Nuclear Polarization of Frozen Solutions by Incorporating Dielectric Particles, *J. Am. Chem. Soc.*, 2014, **136**, 15711–15718.

69 A. Zagdoun, G. Casano, O. Ouari, G. Lapadula, A. J. Rossini, M. Lelli, M. Baffert, D. Gajan, L. Veyre, W. E. Maas, M. Rosay, R. T. Weber, C. Thieuleux, C. Coperet, A. Lesage, P. Tordo and L. Emsley, A Slowly Relaxing Rigid Biradical for Efficient Dynamic Nuclear Polarization Surface-Enhanced NMR Spectroscopy: Expeditious Characterization of Functional Group Manipulation in Hybrid Materials, *J. Am. Chem. Soc.*, 2012, **134**, 2284–2291.

70 T. Sato, Y. Hamada, M. Sumikawa, S. Araki and H. Yamamoto, Solubility of Oxygen in Organic Solvents and Calculation of the Hansen Solubility Parameters of Oxygen, *Ind. Eng. Chem. Res.*, 2014, **53**, 19331–19337.

71 R. Battino, T. R. Rettich and T. Tominaga, The Solubility of Oxygen and Ozone in Liquids, *J. Phys. Chem. Ref. Data*, 1983, **12**, 163–178.

72 A. Venkatesh, G. Casano, Y. Rao, F. De Biasi, F. A. Perras, D. J. Kubicki, D. Siri, S. Abel, H. Karoui, M. Yulikov, O. Ouari and L. Emsley, Deuterated TEKPol Biradicals and the Spin-Diffusion Barrier in MAS DNP, *Angew. Chem., Int. Ed.*, 2023, **62**, e202304844.

73 T. Dubroca, A. N. A. N. Smith, K. J. K. J. Pike, S. Froud, R. Wylde, B. Trociewitz, J. E. McKay, F. Mentink-Vigier, J. van Tol, S. Wi, W. W. Brey, J. R. Long, L. Frydman and S. Hill, A quasi-optical and corrugated waveguide microwave transmission system for simultaneous dynamic nuclear polarization NMR on two separate 14.1 T spectrometers, *J. Magn. Reson.*, 2018, **289**, 35–44.

74 J. van Tol, L.-C. Brunel and R. J. Wylde, A quasioptical transient electron spin resonance spectrometer operating at 120 and 240 GHz, *Rev. Sci. Instrum.*, 2005, **76**, 074101.

75 F. Neese, The ORCA program system, *Wiley Interdiscip. Rev.: Comput. Mol. Sci.*, 2012, **2**, 73–78.

76 M. D. Hanwell, D. E. Curtis, D. C. Lonie, T. Vandermeersch, E. Zurek and G. R. Hutchison, Avogadro: An advanced semantic chemical editor, visualization, and analysis platform, *J. Cheminf.*, 2012, **4**, 1–17.

77 S. Grimme, A. Hansen, S. Ehlert and J.-M. Mewes, $r_2$SCAN-3c: A ''Swiss army knife'' composite electronic-structure method, *J. Chem. Phys.*, 2021, **154**, 064103.

78 A. V. Marenich, C. J. Cramer and D. G. Truhlar, Universal Solvation Model Based on Solute Electron Density and on a Continuum Model of the Solvent Defined by the Bulk Dielectric Constant and Atomic Surface Tensions, *J. Phys. Chem. B*, 2009, **113**, 6378–6396.

79 C. Adamo and V. Barone, Toward reliable density functional methods without adjustable parameters: The PBE0 model, *J. Chem. Phys.*, 1999, **110**, 6158–6170.

80 F. Weigend and R. Ahlrichs, Balanced basis sets of split valence, triple zeta valence and quadruple zeta valence quality for H to Rn: Design and assessment of accuracy, *Phys. Chem. Chem. Phys.*, 2005, **7**, 3297.

81 A. A. Auer, V. A. Tran, B. Sharma, G. L. Stoychev, D. Marx, F. Neese, A. A. Auer, V. A. Tran, B. Sharma, G. L. Stoychev and A. A. Auer, A case study of density functional theory and domain-based local pair natural orbital coupled cluster for vibrational effects on EPR hyperfine coupling constants: vibrational perturbation theory versus ab initio molecular dynamics constants: vibrational, *Mol. Phys.*, 2020, 1–16.

82 E. Caldeweyher, S. Ehlert, A. Hansen, H. Neugebauer, S. Spicher, C. Bannwarth and S. Grimme, A generally applicable atomic-charge dependent London dispersion correction, *J. Chem. Phys.*, 2019, **150**, 154122.

83 N. Mardirossian and M. Head-Gordon, $\omega$B97M-V: A combinatorially optimized, range-separated hybrid, meta-GGA density functional with VV10 nonlocal correlation, *J. Chem. Phys.*, 2016, **144**, 214110.

84 K. Tagami, A. Equbal, I. Kaminker, B. Kirtman and S. Han, Biradical rotamer states tune electron J coupling and MAS dynamic nuclear polarization enhancement, *Solid State Nucl. Magn. Reson.*, 2019, **101**, 12–20.

85 S. Stoll and R. D. Britt, General and efficient simulation of pulse EPR spectra, *Phys. Chem. Chem. Phys.*, 2009, **11**, 6614–6625.

86 P. Eastman, J. Swails, J. D. Chodera, R. T. McGibbon, Y. Zhao, K. A. Beauchamp, L.-P. Wang, A. C. Simmonett, M. P. Harrigan, C. D. Stern, R. P. Wiewiora, B. R. Brooks and V. S. Pande, OpenMM 7: Rapid development of high performance algorithms for molecular dynamics, *PLoS Comput. Biol.*, 2017, **13**, e1005659.

87 C. Tian, K. Kasavajhala, K. A. A. Belfon, L. Raguette, H. Huang, A. N. Migues, J. Bickel, Y. Wang, J. Pincay, Q. Wu and C. Simmerling, ff19SB: Amino-Acid-Specific Protein Backbone Parameters Trained against Quantum Mechanics Energy Surfaces in Solution, *J. Chem. Theory Comput.*, 2020, **16**, 528–552.

88 E. Stendardo, A. Pedone, P. Cimino, M. Cristina Menziani, O. Crescenzi and V. Barone, Extension of the AMBER force-field for the study of large nitroxides in condensed phases: an ab initio parameterization, *Phys. Chem. Chem. Phys.*, 2010, **12**, 11697.

89 X. He, V. H. Man, W. Yang, T.-S. Lee and J. Wang, A fast and high-quality charge model for the next generation general AMBER force field, *J. Chem. Phys.*, 2020, **153**, 114502.

90 F. Hecker, L. Fries, M. Hiller, M. Chiesa and M. Bennati, 17O Hyperfine Spectroscopy Reveals Hydration Structure of Nitroxide Radicals in Aqueous Solutions, *Angew. Chem., Int. Ed.*, 2023, **62**, e202213700.

91 T. Lu and F. Chen, Multiwfn: A multifunctional wavefunction analyzer, *J. Comput. Chem.*, 2012, **33**, 580–592.

92 H. Sato, V. Kathirvelu, A. Fielding, J. P. Blinco, A. S. Micallef, S. E. Bottle, S. S. Eaton and G. R. Eaton, Impact of molecular size on electron spin relaxation rates of nitroxyl radicals in glassy solvents between 100 and 300 K, *Mol. Phys.*, 2007, **105**, 2137–2151.

93 V. Kathirvelu, C. Smith, C. Parks, M. A. Mannan, Y. Miura, K. Takeshita, S. S. Eaton and G. R. Eaton, Relaxation rates for spirocyclohexyl nitroxyl radicals are suitable for inter-spin distance measurements at temperatures up to about 125 K, *Chem. Commun.*, 2009, (4), 454–456.

94 A. P. Jagtap, M.-A. Geiger, D. Stöppler, M. Orwick-Rydmark, H. Oschkinat and S. T. Sigurdsson, bcTol: a highly water-soluble biradical for efficient dynamic nuclear polarization of biomolecules, *Chem. Commun.*, 2016, **52**, 7020–7023.

95 I. A. Kirilyuk, Y. F. Polienko, O. A. Krumkacheva, R. K. Strizhakov, Y. V. Gatilov, I. A. Grigor'ev and E. G. Bagryanskaya, Synthesis of 2,5-Bis(spirocyclohexane)-Substituted Nitroxides of Pyrroline and Pyrrolidine Series, Including Thiol-Specific Spin Label: An Analogue of MTSSL with Long Relaxation Time, *J. Org. Chem.*, 2012, **77**, 8016–8027.

96 G. Stevanato, G. Casano, D. J. Kubicki, Y. Rao, L. E. Hofer, G. Menzildjian, H. Karoui, D. Siri, M. Cordova, M. Yulikov, G. Jeschke, M. Lelli, A. Lesage, O. Ouari and L. Emsley, Open and Closed Radicals: Local Geometry around Unpaired Electrons Governs Magic-Angle Spinning Dynamic Nuclear Polarization Performance, *J. Am. Chem. Soc.*, 2020, **142**, 33.

97 J. Soetbeer, P. Gast, J. J. Walish, Y. Zhao, C. George, C. Yang, T. M. Swager, R. G. Griffin and G. Mathies, Conformation of bis-nitroxide polarizing agents by multi-frequency EPR spectroscopy, *Phys. Chem. Chem. Phys.*, 2018, **20**, 25506–25517.

98 M. A. Geiger, A. P. Jagtap, M. Kaushik, H. Sun, D. Stöppler, S. T. Sigurdsson, B. Corzilius and H. Oschkinat, Efficiency of Water-Soluble Nitroxide Biradicals for Dynamic Nuclear Polarization in Rotating Solids at 9.4 T: bcTol-M and cyolyl-TOTAPOL as New Polarizing Agents, *Chem. – Eur. J.*, 2018, **24**, 13485–13494.

99 S. R. Chaudhari, D. Wisser, A. C. Pinon, P. Berruyer, D. Gajan, P. Tordo, O. Ouari, C. Reiter, F. Engelke, C. Copéret, M. Lelli, A. Lesage and L. Emsley, Dynamic Nuclear Polarization Efficiency Increased by Very Fast Magic Angle Spinning, *J. Am. Chem. Soc.*, 2017, **139**, 10609–10612.

100 P. Negrier, M. Barrio, J. L. Tamarit, D. Mondieig, M. J. Zuriaga and S. C. Perez, Conformational Polymorphism: The Missing Phase of 1,1,2,2-Tetrachloroethane ($Cl_2HC–CHCl_2$), *Cryst. Growth Des.*, 2013, **13**, 2143–2148.

101 M. Wolska-Pietkiewicz, A. Grala, I. Justyniak, D. Hryciuk, M. Jędrzejewska, J. Grzonka, K. J. Kurzydłowski and J. Lewiński, From Well-Defined Alkylzinc Phosphinates to Quantum-Sized ZnO Nanocrystals, *Chem. – Eur. J.*, 2017, **23**, 11856–11865.

102 D. Lee, M. Wolska-Pietkiewicz, S. Badoni, A. Grala, J. Lewiński and G. De Paëpe, Disclosing Interfaces of ZnO Nanocrystals Using Dynamic Nuclear Polarization: Sol-Gel versus Organometallic Approach, *Angew. Chem., Int. Ed.*, 2019, **58**, 17163–17168.

 